Photoassociative spectroscopy of highly excited vibrational levels of alkali-metal dimers: Green-function approach for eigenvalue solvers

Eite Tiesinga,* Carl J. Williams,[†] and Paul S. Julienne

Atomic Physics Division, National Institute of Standards and Technology, Gaithersburg, Maryland 20899

(Received 18 December 1997)

Understanding high-precision photoassociative spectroscopy of laser-cooled alkali-metal atoms involves modeling an extremely dense level structure of weakly bound molecules in the region where coriolis and hyperfine interactions become comparable to electronic interactions. We describe an iterative eigenvalue solver suitable for resolving these bound states that is based on finding eigenvalues of the shifted inverse or Green-function operator. Nonlinear coordinate transformations applied to the nuclear motion are introduced to minimize the dimensionality of the discretized Hamiltonian. The formalism is applied to resolve the hyperfine structure of rovibrational levels of the $Na(^2P) + Na(^2S)$ dimer. [S1050-2947(98)05306-2]

PACS number(s): 33.15.Pw, 33.20.Wr, 02.60.Dc, 02.70.−c

I. INTRODUCTION

In recent years laser cooling has made samples of ultra-cold atoms routinely available. Stored in magneto-optical (MOT) or pure magnetic traps the study of collisional processes between two trapped atoms, either via direct measurements of cross sections or via photoassociation is a logical course of action [1–3]. The temperatures in the various traps are so low, below 1 mK for MOT's and even in the nanokelvin range for magnetic traps, that many of the measurable collision quantities are dominated by long-range forces. For example, the shape of the macroscopic wave function of a Bose-Einstein condensate of a magnetically stored sample of ^2S alkali-metal atoms [4–6] is determined to a large extent by the scattering length, the effective hard-sphere radius of a zero-energy atom-atom collision. Significant contributions to the scattering length arise from the radial region where the $-C_6/R^6$ van der Waals interaction dominates the atom-atom interaction.

In photoassociation spectroscopy [7–15] a laser photon is used to excite a pair of free ^2S alkali-metal atoms to a vibrational level of the electronic $P+S$ manifold. This vibrational state is then detected by either looking for fluorescence or by detecting ions after absorption of another photon. For the small collision energies prevailing in a MOT the Franck-Condon principle predicts the formation of long-range molecules, with outer turning points around internuclear separations of 10 nm and inner turning points of the vibrational motion as small as 0.2 nm. Therefore this process is not only sensitive to the van der Waals potential between the two colliding atoms but also to the $\pm C_3/R^3$ resonant-dipole interaction of the excited molecule.

Recently in an experimental collaboration we have extracted the long-range C_3 coefficient for Na ^2P + Na ^2S from binding energies of rovibrational levels of the purely long-range 0_g^- potential close to the $^2P_{3/2}+^2S$ dissociation limit [13]. The extraction of the C_3 coefficient, which provides the most accurate measurement to date of the Na ^2P atomic lifetime, is based on a precise knowledge of the dynamics of the long-range $^2P+^2S$ molecule. We have shown that the finite speed of the photon, which is resonantly exchanged between the two Na atoms, is observable in the photoassociation spectra as a retardation correction. In addition, a detailed knowledge of the influence of atomic hyperfine and coriolis interactions on the 0_g^- rotational-vibrational levels is essential [16]. An understanding of these weak interaction terms lead to simplifying models of the 0_g^- state [13,16].

For the measurement of the Na C_3 coefficient from the experimental 0_g^- spectra hyperfine corrections were neglected. This approximation was justified by comparing with numerical eigenvalues and eigenfunctions of the exact Hamiltonian of the dimer as well as from a comparison with simplifying models [16]. In this paper we provide a concise description of the numerical procedures used in the exact calculations. The procedures are not limited to the Na dimer but can be used in understanding hyperfine resolved spectra of all other alkali species. The discretization of the Hamiltonians, which involves a large number of spins degrees of freedom as well as a large number collocation points to describe the radial coordinate, leads to a large-scale eigenvalue problem. In fact, minimizing the size of the matrices is essential to successfully solving the eigenvalue problem and warrants a detailed discussion. Moreover, the eigenvalues of interest are in the middle of the spectral range as well as in a region where the eigenvalues are most densely packed, i.e., near a dissociation limit. The numerical methods for solving these type of problems are actively discussed in the literature [17–20]. These numerical methods are based on an iterative eigenvalue solver where a matrix-vector multiplication of the discretized Hamiltonian with an arbitrary vector (wave function) and a filtering process, that makes the solver converge to eigenfunctions near the eigenvalues of interest, must be provided by the user. The filter is based upon an approximation to the full problem that can be handled by more conventional means. In this paper we describe our experience using the iterative eigenvalue solver proposed in Ref. [20] as well

---

*Permanent address: Department of Chemistry and Biochemistry, University of Maryland, College Park, MD 20742.

[†]Permanent address: Institute for Defense Analysis, 1801 N. Beauregard St., Alexandria, VA 22311-1772.

as discuss the physical approximations valid for $P+S$ systems that enable the construction of a practical filter. Although we focus on $P+S$ systems where we can identify strong and weak interactions and therefore can construct (much) smaller subproblems, many quantum-mechanical systems have such a division and similar iterative eigenvalue solvers can be applied.

Previous work on theoretical modeling of photoassociation spectroscopy is restricted to a description of the vibrational levels of the long-range 0_g^- state in the last hundred GHz below the $^2P_{3/2}+{}^2S$ dissociation limit. However, the experimental photoassociation spectra show a far richer picture. Other vibrational series, like the so-called 1_g and 0_u^+ series, interleave with the rovibrational series of the 0_g^- state. Unlike the 0 states, which have no hyperfine structure on their own, the 1_g series has a marked hyperfine structure, which becomes comparable to and even larger than the rotational spacing. The resulting density of state suggests that approximately 10% of the Na $^2P+$Na ^2S bound states are in the last hundred GHz below dissociation. In addition to the 0_g^- states the iterative eigenvalue solver also finds these states, which opens up the study of these states as well as a study of their mixing very close to the dissociation limit.

This paper is divided into four sections. In Sec. II we discuss the discretization of the radial coordinate. Section III describes coordinate transformations that dramatically reduce the number of collocation points that are needed for the accurate description of the vibrational motion. Section IV gives a description of the eigenvalue solver and discusses the requirements on the nature of the filter in our implementation of the eigenvalue solver. The section also discusses some parallel programming issues. Finally in Sec. V the iterative eigenvalue solver is used to perform a state-of-the-art calculation of the bound states of $P+S$ Na$_2$ dimers. The effectiveness of the coordinate transformation is demonstrated by investigating the convergence of the bound-state binding energies for a single potential with respect to the number of collocation points. A practical filter for the eigenvalue solver is also constructed and some results from exact calculations are presented and discussed.

II. DISCRETIZATION

The structure of the Hamiltonian for diatomics is typical for a large class of quantum mechanical systems. It consists of a kinetic energy term $T=-(\hbar^2/2\mu)d^2/dR^2$, where R is the distance between two nuclei and μ is the reduced atomic mass, and an interaction term V. The kinetic energy operator introduces coupling between different internuclear separations and the interaction potential V represents a set of coupled potential surfaces at each R. Each potential surface is labeled by a set of spin quantum numbers or symmetry labels. The multichannel eigenstates $|\Psi\rangle$ of the Hamiltonian are given by $\Sigma_\alpha \int dR \Psi_\alpha(R)|R\alpha\rangle$, where the α's label the spin degrees of freedom. A discrete variable representation (DVR) [21] of the Hamiltonian inherits the simple structure of T and V and is a natural choice for discretization of the Hamiltonian. That is, the numerical calculations use the basis $|R_i\alpha_j\rangle$ where the indices i and j count the radial points and spin states, respectively, so that the Hamiltonian is represented by

$$H_{\{ij\},\{i'j'\}}=T_{ii'}\delta_{jj'}+\delta_{ii'}V_{ijj'},$$

where the quantity $V_{ijj'}$ is short for $V_{jj'}(R_i)$. The DVR representation is closely related to the more familiar finite basis representation (FBR).

The simplest DVR is the Fourier grid representation [22], which was, for example, employed in Ref. [23] to study nonadiabatic effects in the dynamics of the alkali-metal dimers, and is based on the eigenfunctions of a particle in a box. The DVR has equidistant collocation points R_i and an analytic expression for the kinetic energy operator. In the interval (R_0,R_N) with $N-1$ collocation the points have the form

$$R_i=R_0+(R_N-R_0)i/N, \quad i=1 \text{ to } N-1$$

the kinetic energy operator is given by

$$T_{ii'}=\frac{\hbar^2}{2\mu}\frac{\pi^2(-1)^{i-i'}}{2(R_N-R_0)^2}\left\{\frac{1}{\sin^2[\pi(i-i')/2N]}\right.$$
$$\left.-\frac{1}{\sin^2[\pi(i+i')/2N]}\right\} \quad (1)$$

for $i\neq i'$ and

$$T_{ii}=\frac{\hbar^2}{2\mu}\frac{\pi^2}{2(R_N-R_0)^2}\left\{\frac{2N^2+1}{3}-\frac{1}{\sin^2(\pi i/N)}\right\} \quad (2)$$

for $i=i'$.

III. COORDINATE TRANSFORMATION

For the weakly bound long-range dimers produced in an ultracold photoassociation experiment the typical values for R_0 and R_N are 0.2 and 20 nm, although in some cases R_N can be much larger. These values are roughly determined by the inner and outer turning points of the vibrational wave functions. The minimum step size $\Delta R_{min}=(R_N-R_0)/N$ is determined by the kinetic energy at the internuclear separation where the potential V is most deep. In fact, the value for ΔR_{min} must be smaller than local de Broglie wavelength of the wave function near this internuclear separation. For alkali dimers this internuclear separation is around 0.4 nm very close to R_0 where the depth of the potentials is typically about 10^5 GHz and hence the number of radial collocation points needed between R_0 and R_N can easily exceed 10^4. Moreover, this number must be multiplied with the number of spin states α in order to obtain the total dimension of the Hamiltonian matrix. This quickly leads to unmanageable eigenvalue problems.

For large internuclear separations the local de Broglie wavelength is much larger than near the deepest point of the potential, which implies that for those regions the grid is unnecessarily dense. Two approaches to reduce the number of collocation points suggest themselves. The first possibility is based on a more complex DVR, such as the Gauss-Hermite DVR based on the eigenfunctions of the harmonic oscillator or the Sturmian DVR based on orthonormal Sturmian polynomials [17,21]. In both cases the grid is inhomogeneous and the step size grows roughly linearly with inter-

nuclear separation. Unlike the Fourier grid DVR the kinetic energy operator has to be calculated numerically, but these DVR's do lead to a significant reduction of the number of collocation points.

A second approach, based on nonlinear coordinate transformations, is adopted for this work and leads to the smallest possible matrix dimensions. The transformation is given by $y = u(R)$ where u is a monotonic invertible function of R with a derivative that decreases with increasing R. Therefore, by defining a homogeneous grid in the transformed y coordinate the distance between two collocation points in the original coordinate grows with increasing R. For example, the logarithmic transformation $y = \ln R$, often used in atomic electronic structure calculations, gives a step size that grows linearly with R. Therefore a logarithmic transformation leads to a grid that has features similar to the Gauss-Hermite or Sturmian DVR. However, unlike these complex DVR's, which are based on the existence of a suitable orthogonal polynomial, coordinate transformations are more flexible as they can be chosen to reflect a physical problem more closely.

The coordinate transformation promises to be a good candidate for minimizing the matrix dimensions but will also modify the kinetic energy operator of the Hamiltonian. Below it is shown that this transformed differential operator can be discretized without sacrificing the advantages of a discrete variable representation. The kinetic-energy operator transforms into

$$T = -\frac{\hbar^2}{2\mu}\frac{d^2}{dR^2} = -\frac{\hbar^2}{2\mu}\left\{ p(y)\frac{d^2}{dy^2} + q(y)\frac{d}{dy} \right\} \quad (3)$$

with

$$p(y) = \frac{1}{[U'(y)]^2} \quad \text{and} \quad q(y) = -\frac{U''(y)}{[U'(y)]^3}, \quad (4)$$

where $U(y)$ is the inverse transformation of u. It is convenient to introduce a simultaneous wave-function transformation that has the property that it preserves the normalization. That is we introduce $\phi(y)$ with

$$\Psi(R) = \frac{\phi(y)}{\sqrt{U'(y)}}, \quad (5)$$

and therefore if Ψ is normalized with respect to R the transformed wave function ϕ is normalized with respect to y. The total Hamiltonian $T + V$ is finally given by

$$\left[\frac{\hbar^2}{2\mu}\left\{ -\frac{1}{U'(y)}\frac{d^2}{dy^2}\frac{1}{U'(y)} - \frac{1}{2}\frac{U^{(3)}(y)}{[U'(y)]^3} \right.\right.$$
$$\left.\left. + \frac{3}{4}\frac{[U''(y)]^2}{[U'(y)]^4} \right\} + \tilde{V}(y) \right]\phi(y) = E\phi(y), \quad (6)$$

where $\tilde{V}(y) = V(U(y))$. The first term on the left-hand side of this equation can be interpreted as the new kinetic energy operator and the second and third terms behave as additional spin-independent potentials. These potentials are analogous

to the "centrifugal term" of the untransformed Schrödinger equation. For example, if $u(R) \propto R^\beta$ for $R \to \infty$ with $\beta \leq 1$, these new potentials are proportional to $1/R^2$. The Fourier grid DVR, as defined in Eqs. (1) and (2), can be used to discretize d^2/dy^2 but now on the homogeneous grid $y_i = y_0 + (y_N - y_0)i/N$. The terms containing derivatives of U and the potential term $\tilde{V}$ are diagonal in y_i.

The nonlinear coordinate transformation has been introduced as a means of reducing the number of collocation points at large R. A different perspective on the transformation suggests a way of determining the optimal transformation. The WKB solution of a bound state for a single potential surface in the classically allowed region is given by

$$\Psi(R) = \frac{1}{\sqrt[4]{|\mathcal{E} - V(R)|}}\sin\left(\int^R dx\sqrt{2\mu/\hbar^2[\mathcal{E} - V(x)]} \right), \quad (7)$$

where $\mathcal{E}$ is the binding energy. The phase of this wave function in the transformed coordinate y is given by

$$\int^y dy\, U'(y)\sqrt{2\mu/\hbar^2[\mathcal{E} - \tilde{V}(y)]}. \quad (8)$$

By equating $U'(y) = 1/\sqrt{2\mu/\hbar^2[\mathcal{E} - \tilde{V}(y)]}$ the phase of the wave function is $y - \zeta_0$, where ζ_0 is an arbitrary phase that depends on the details of the potential and we find that the transformed wave function $\phi(y)$ is proportional to $U'(y)\sin(y - \zeta_0)$. The wave function ϕ is a fast oscillating sine with a single frequency times a slowly varying envelope $U'(y)$ and therefore a homogeneous grid in y will provide a suitable grid for all internuclear separations.

The transformation $u(R) \propto \int^R dx\sqrt{\mathcal{E} - V(x)}$ is therefore ideal for reducing the number of collocation points needed to determine bound states near the energy $\mathcal{E}$ for single potential. In a multichannel environment, with many coupled potential surfaces, the deepest curve is a natural choice for $V(x)$. However, the transformation is often impractical as its inverse is not easily found or even nonexistent. An analytic alternative is based on the long-range dependence C_n/R^n of the potentials and using $\mathcal{E} \approx 0$ for bound states near the dissociation limit. In that limit the transformation is

$$u(R) = \int_R^\infty \frac{dx}{R_0}\sqrt{\left(\frac{R_0}{x + R_s}\right)^n} = -\frac{1}{n/2 - 1}\left(\frac{R_0}{R + R_s}\right)^{n/2 - 1}, \quad (9)$$

where the n is the leading polynomial degree of the long-range tail of the potentials and R_0 and R_s are free parameters, although $R_0 \approx (2\mu C_n/\hbar^2)^{1/(n-2)}$ is a good initial guess. The transformation ensures that for large internuclear separations the step size in the untransformed basis will increase at the same rate as the local de Broglie wavelength. For a resonant dipole interaction ($n = 3$) the step size increases as $(R + R_s)^{3/2}$. Deviations from a pure $1/R^n$ behavior at smaller internuclear separation, the position of the deepest part of the potentials, and specific multichannel effects such as multiple values of C_n determine the best values of R_0 and R_s.

In order to understand the discussion in the next sections it is useful to briefly mention realistic values for the matrix size. For the Na dimer the use of a coordinate transformation limits the number of collocation points for the nuclear motion to ~ 500 and there are approximately 100 spin channels leading to a total matrix size of 5×10^4. A discussion and justification of these numbers is found in Sec. V.

IV. FILTERING

For a large eigenvalue problem, with dimension of 5×10^4 or larger, the use of iterative methods is inevitable. However, these methods are best suited for finding extreme eigenvalues that are not too closely packed, which is in contrast with the requirements for vibrational levels near the dissociation limit. These conflicting requirements are met by solving for the lowest or highest eigenvalues of the ''Green-function'' filter $G = 1/(\mathcal{E} - H)$ where the energy $\mathcal{E}$ determines the spectral region in which eigenvalues are found. An eigenvalues solver such as the implicitly restarted Lanczos algorithm [24] can then be used to find the eigenvectors of G iteratively. This algorithm requires the calculation of the matrix vector multiplication Gx where x is some arbitrary vector. This does not imply that the filter has to be formed explicitly. It suffices to construct an iterative means to solve for Gx. In fact, the matrix-vector multiplication is equivalent to solving for the linear system $(\mathcal{E} - H)z = x$, which can be solved iteratively [25]. However, the initial difficulty of converging the iterative eigenvalue solvers when there is a high density of states near $\mathcal{E}$, is still present. Convergence for the iterative linear system solver can only be obtained if the linear system is multiplied with a so-called preconditioner (G_0). That is we need to solve the linear system

$$G_0(\mathcal{E} - H)z = G_0 x. \tag{10}$$

The purpose of the preconditioner is to transform the operator on the left hand side of the equation into an operator that is as close as possible to the unit operator but at the same time remains easy to compute. In fact, G_0 behaves like an approximation of G since Eq. (10) can be rewritten as

$$z = [1 + G_0 H_1 + (G_0 H_1)^2 + \cdots] G_0 x, \tag{11}$$

where H_0 is an approximation of H, $G_0 = 1/(\mathcal{E} - H_0)$, and $H_1 = H - H_0$ is the ''potential.'' This connects Eq. (10) with the ''physical'' Lippmann-Schwinger equation for bound states. In fact Eq. (11) can be used to evaluate Eq. (10). Convergence of this Neumann polynomial, however, is only guaranteed if the product $G_0 H_1$ is small in terms of some matrix norm. The generalized minimal residual (GMRES) method [25] is a good alternative to the Neumann polynomial and has the fastest convergence characteristic of all known linear system solvers. GMRES of order n is based on finding the best solution z within the subspace spanned by the basis set $\{z_i = [G_0(\mathcal{E} - H)]^i x, \ i = 1, \ldots, n\}$ by minimizing the length of the residual vector $G_0(\mathcal{E} - H)z - G_0 x$ within this basis. This feature also demonstrates the major drawback of GMRES that all vectors z_i need to be stored. Again the ability to construct a good preconditioner G_0 is essential as it keeps the value of n needed to reach convergence as small as possible.

To help construct a suitable preconditioner for the alkali-metal dimer problem we have taken advantage of a new class of parallel computers that use communication libraries like PVM (Parallel Virtual Machine), MPL (Message Passing Library), or MPI (Message Passing Interface), which allow the user to construct their own communication pattern between the independent processors of any networked computer cluster. In order to use some of the parallel capabilities of these libraries we assume that the preconditioner G_0 has a block structure, i.e., has independent subspaces. This is a minor restriction since in many physical problems with both weak and strong interactions the neglect of the weak interactions often reduces the Hamiltonian H to a block diagonal structure H_0. The different subspaces/blocks need not have the same dimensionality and can be distributed over the nodes of the virtual machine, which in our case is a loosely connected set of UNIX workstations. Each node is responsible for calculating G_0 for one or more subspaces. This can be done by calculating $1/(\mathcal{E} - H_0)$ for each small block via direct inversion or diagonalization [26]. The advantage of this procedure is that sophisticated approximations can be chosen that otherwise would quickly lead to storage requirements that are too large for a single computer. For the bound states of the Na dimer there are approximately 30 blocks where each block is of the order 1500×1500. A detailed discussion of these components of G_0 is given in the following section.

The Lanczos eigenvalue solver and the GMRES software are standard serial codes that run on a single computer node. Therefore, the parallelism is limited to the evaluation of G_0 and the formation of the matrix-vector multiplication $G_0 x$ using a ''master-slave'' communication protocol. The master node runs the two serial codes while the slaves store the different blocks that build G_0. Moreover, the master continuously asks the slaves to multiply their part of G_0 with a vector x. At the end of the calculation the extreme eigenvalues f_i and the corresponding eigenvectors of G are returned by the Lanczos eigenvalue solver and the eigenvalues of H are constructed using $E_i = \mathcal{E} + 1/f_i$. The accuracy of the normalized eigenvectors Ψ_i of the Hamiltonian are checked using

$$\Delta = \sqrt{|\langle \Psi_i | H^2 | \Psi_i \rangle - (\langle \Psi_i | H | \Psi_i \rangle)^2|}. \tag{12}$$

This quantity is a conservative upper bound to the accuracy of each eigenvalue and reflects the contamination of the approximate numerical eigenvector with nearby lying mathematical eigenstates. The error that follows from Eq. (12) describes the ability of the eigenvalue solver to converge the eigenvalue for a given radial grid. It should not be confused with the convergence with respect to the radial step size and length of the grid. Those issues are discussed in Sec. V A and the last paragraph of Sec. V B.

V. THE SODIUM DIMER

We apply the Green-function code to find the hyperfine resolved rovibrational bound states of a sodium dimer near the $^2P + ^2S$ dissociation limit. These molecules can be formed from a laser-cooled sample of ^2S atoms by absorption of a single photon, a photoassociation experiment [2]. Typically these molecules have an outer vibrational turning

point between 2.5 and 20 nm depending on the detuning of the photon from dissociation. At these internuclear separations chemical effects, due to electron cloud overlap between the individual atoms, are negligible. In fact, it is convenient to describe these molecules as the collision between two atoms.

For the ^2P atom the atomic Hamiltonian involves the strong spin-orbit interaction and the hyperfine interaction. The former couples the electron mechanical angular momentum, l_a, to the electron spin, s_a, and forms the electron angular momentum $\vec{j}_a = \vec{l}_a + \vec{s}_a$ while the hyperfine interaction couples the electron angular momentum to the nuclear spin, i_a. The ^2S atom has zero electron mechanical angular momentum, l_b, and the atomic Hamiltonian only includes the atomic hyperfine interaction where the electron spin, s_b, couples to the nuclear spin, i_b. The subscript $\alpha = a$ and b for spin degrees of freedom will always denote the ^2P and ^2S atom, respectively. The two atoms are allowed to rotate around their center of mass generating the interaction $\hbar^2 \vec{l}^2 / 2\mu R^2$, where the operator $\vec{l}$ is the mechanical angular momentum between the two nuclei. By definition l has a zero projection onto the internuclear axis. In this manner a complete basis is constructed using $|l j_a (f_a f_b) f; FM, p\rangle$, where $\vec{f}_\alpha = \vec{j}_\alpha + \vec{i}_\alpha$, and $\vec{f} = \vec{f}_a + \vec{f}_b$. These kets form states with total angular momentum $\vec{F}$, the vector sum of $\vec{l}, \vec{s}_a, \vec{i}_a, \vec{l}_a, \vec{s}_b$, and $\vec{i}_b$, and have a definite parity $p = \Pi_a \Pi_b (-1)^l$ where $\Pi_a(\Pi_b)$ are the parity of atom a (b), respectively. In our case $\Pi_a = 1$ and $\Pi_b = -1$. Note that $l_b = 0$ for the ^2S atom has been omitted for convenience and in the absence of external fields both $F = 0,1,2,\ldots,M$, and the parity are conserved. This is the atomic or Hund's case (e) basis set.

The fine structure and hyperfine interaction are diagonal in the atomic basis. Since ^2S and ^2P Na have an electron spin of 1/2 and a nuclear spin of 3/2, twelve distinct asymptotic energies for the dimer exist as is shown in Fig. 1. The fine structure splitting gives a 513-GHz separation between $j_a = 1/2$ and 3/2 states. The hyperfine splitting of the ^2S atom separates the $f_b = 1$ and 2 states by 1.8 GHz, while the hyperfine interaction of the ^2P atom is ≈ 0.2 GHz and splits states with $f_a = 1$ or 2 for the $^2P_{j_a = 1/2}$ atom and $f_a = 0, 1, 2$, or 3 for the $^2P_{j_a = 3/2}$ atom. Quadrupole effects for the $^2P_{3/2}$ atom, which are on the order of 1 MHz, may also be included. Each asymptote is degenerate with respect to the projections of f_a and f_b. For example, the limit $^2P_{3/2}(f_a = 3) + {}^2S(f_b = 1)$ is $7 \times 3 \times 2 = 42$-fold degenerate. The extra factor of two comes from homonuclear symmetrization, which accounts for the fact that $P + S$ states are degenerate with those of $S + P$. In total there are 384 states, however, for a given F and parity at most 96 spin channels are interacting. These values for fine and hyperfine splittings are meant as guidelines. Calculations in the remainder of the paper use the accurate values of Ref. [27].

In addition to the atomic interactions, the two atoms undergo molecular-type interactions caused by the residual effect of all Coulombic interactions between the particles. At large internuclear separations these reduce to the resonant dipole interaction [28], which couples the electric dipole moment of both atoms to the internuclear axis and has a radial
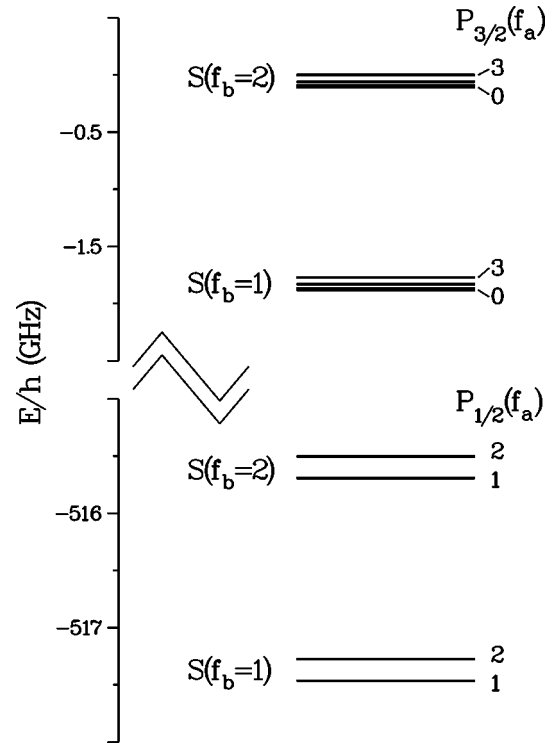
FIG. 1. The twelve distinct asymptotic limits of a Na(^2P) + Na(^2S) collision. The zero of energy is set at the $^2P_{3/2}(f_a = 3) + {}^2S(f_b = 2)$ asymptote. All multichannel eigenvalues in this paper are quoted with respect to this asymptote.

dependence given by $1/R^3$. The resonant dipole interaction conserves the projection Λ of the spin $\vec{L} = \vec{l}_a + \vec{l}_b$ onto the internuclear axis and conserves the total electron spin $\vec{S} = \vec{s}_a + \vec{s}_b$, the total nuclear spin $\vec{I} = \vec{i}_a + \vec{i}_b$, and for homonuclear dimers the symmetry of the electronic part of the wave function under inversion around the center of mass, i.e., g/u symmetry. This results in four nondegenerate potential surfaces corresponding to the $\Lambda = 1$ (Π) states with an $\pm C_3 / R^3$ radial dependence and the $\Lambda = 0$ (Σ) states with a $\pm 2 C_3 / R^3$ dependence. For internuclear separations where the electron clouds of the two atoms overlap the exchange interaction splits each of the four surfaces into two, leading to eight distinct (nonrelativistic) adiabatic Born-Oppenheimer (ABO) potentials labeled by $^{2S+1}\Lambda_{g/u}$. The natural basis for the resonant dipole interaction is a molecular basis, labeled as $|\Lambda S \Sigma I \iota F M, p\rangle_\sigma$, where $\sigma = g/u$, Σ and ι are the projections of S and I on the internuclear axis, respectively. This basis is the so-called Hund's case (a) basis and for homonuclear diatomics only includes states with $p = \rho(-1)^l$ and with $\rho = 1$ or -1 for g or u states, respectively. The inset of Fig. 2 shows the eight ABO potentials for small internuclear separations where they control the dynamics of the vibrational motion of the dimer.

The molecular Hund's case (a) and atomic Hund's case (e) bases provide a diagonal representation of the molecular and atomic contributions to the Hamiltonian, respectively. The two bases are connected via an unitary transformation such that the multichannel vibrational eigenfunctions can be expressed and calculated in either basis. The unitary transformation is evaluated in a manner similar to Refs. [29,30]. The remainder of this paper is devoted to the evaluation of
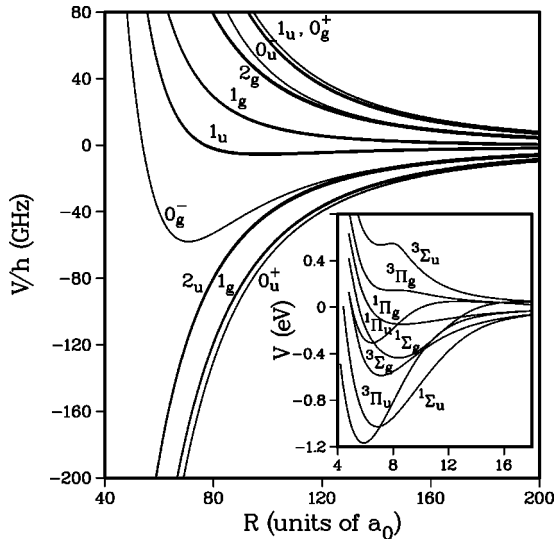
FIG. 2. The long-range adiabatic Movre-Pichler potential curves near the two $S+P_{3/2}$ asymptotes. The labeling follows the Hund's case (c) coupling case. The inset shows the ABO potentials in the radial region where they are the dominant interaction. The labels used in the inset are Hund's case (a) labels. (1 eV = 2.417 988 35 10^5 GHz, $1a_0 = 0.052\,9177$ nm.)

FIG. 3. The convergence of the $^3\Pi_u$ bound states as a function of the number of collocation points. The radial grid runs from $3a_0$ to $550a_0$ with an inhomogeneous grid discussed in the text. The binding energies of the run using $N=1717$ collocation points are assumed to be converged.

the eigenpairs. In Sec. V A the eigenpairs of a single ABO are evaluated in order to test the effectiveness of the radial transformation. In Sec. V B the full calculations are presented. This section also involves a discussion of useful approximations of the dynamics of the dimer as this allows for the construction of a preconditioner G_0 to the eigenvalue problem.

A. Convergence for a single ABO

The effectiveness of the nonlinear coordinate transformation is most dramatically shown by the convergence of the bound state energies for a single potential surface. The eigenvalue problem for a single potential is small compared to multichannel eigenvalue problem and can be solved with noniterative means. The convergence test is performed on the deepest Na ABO potential. This potential has bound-state wave functions with the largest and most rapid changes in size of the local de Broglie wavelength of all the Na ABO's when going from small to large internuclear separation and hence its convergence should ensure convergence of the multichannel bound states of the Na dimer.

For Na the deepest potential is the $^3\Pi_u$ adiabatic Born-Oppenheimer potential (see the inset of Fig. 2). The long-range behavior of this ABO is proportional to $1/R^3$ and therefore following Eq. (10) the transformation $u(R) = -\sqrt{R_0/(R+R_S)}$ is used. We have used $R_S = 3a_0$ ($1a_0 = 0.0529\,177$ nm), $R_0 = 0.5a_0$, and $3a_0$ and $550a_0$ for the first and last point of the grid, respectively, with different numbers of collocation points N. A doubling of the number of collocation points implies that the local step size in R space decreases by a factor of two. The results of this study are shown in Fig. 3. The error as a function of vibrational level is defined as the difference in binding energy with the energies obtained from the finest grid. For $N=428$ the local step size Δr varies from $0.08a_0$ at $10a_0$, $1.0a_0$ at $70a_0$, to
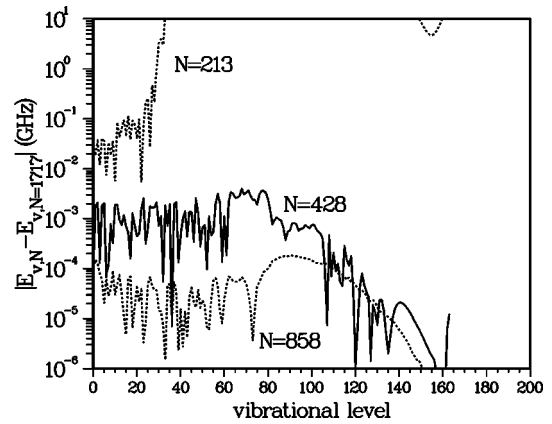
$21a_0$ at $550a_0$. The convergence rate with N is dramatic as one might expect for a high-order DVR approximation of the kinetic energy operator. The largest error occurs around vibrational level 80, which is bound by $-18\,000$ GHz and has an outer turning point of $14a_0$. This is a short-range molecule, since at these internuclear separations the electronic clouds overlap. The levels $v > 130$ close to the dissociation limit converge fastest because the coordinate transformation is optimized for the vibrational motion at large internuclear separations. Moreover, the wave functions of the most weakly bound states for $R_N = 550a_0$ and $N=428$ have on average two to three points per local de Broglie wavelength.

By using $R_N = 550a_0$ we obtained well converged eigenenergies of the $^3\Pi_u$ potential for the 163 vibrational levels which are bound by more than 0.2 GHz. To obtain more weakly bound states (~ 1 MHz) would require changing R_N from $550a_0$ to $20\,000a_0$. However, the nonlinear coordinate transformation ensures that the binding energy of these extremely long-range molecules can be converged by adding no more than 100 collocation points. Even though increasing R_N is feasible we focused on $R_N = 550a_0$ as all the bound states of experimental interest can already be obtained accurately.

For the calculations in the remainder of this paper we chose $N=428$ as the uncertainties in the calculation of the binding energy for long-range molecules lies well below the cited experimental accuracies [13], which are on the order of several MHz.

B. Multichannel calculations

The single-channel results of the previous section show that the radial coordinate, which is of infinite dimensionality, is discretized satisfactorily with only a few hundred collocation points. Since Na has a maximum of 96 spin states, the discretized Hamiltonian H can have a dimension as large as $40\,000 \times 40\,000$. This matrix can only be diagonalized iteratively, and constructing a suitable preconditioning G_0 requires a knowledge of the weak and strong coupling forces between spin channels.

TABLE I. GMRES(n)-convergence statistics as a function of binding energy, total angular momentum $\mathbf{F}$, and preconditioning. The vibrational energy is with respect to the $P_{3/2}(f_a=3)+S(f_b=2)$ asymptote and DOS stands for density of states. Note that the lowest vibrational level is at -3×10^5 GHz from dissociation and the acronym NC stands for not converged.

Energy (GHz)	$F=5$ DOS (GHz^{-1})	$G_{\rm ave}$				G_0			
		$F=0$	$F=3$	$F=5$	$F=6$	$F=0$	$F=3$	$F=5$	$F=6$
-1000	1	8	16	18	NC	7	15	17	19
-50	8	10	18	34	NC	9	16	33	41
-25	16	10	21	30	NC	10	20	30	34
-5	48	23	77	85	NC	20	71	75	71
-3	75	39	147	239	NC	36	137	138	125

For deeply bound vibrational levels the eight ABO potentials provide a good first-order picture of the physics. However, these potentials dissociate to the barycenter energy of the $^2P+^2S$ atomic limit and not to the $^2P_{1/2}+^2S$ or $^2P_{3/2}+^2S$ fine-structure asymptotes and so the ABO's form a poor description for long-range molecule. Movre and Pichler [28] showed that the adiabatic potentials constructed by diagonalizing at each R, the resonant dipole interaction and the atomic fine structure of the ^2P atom, form a good description of the long-range behavior. The adiabatic potentials, dissociating to the $^2P_{3/2}+^2S$ asymptote, are shown in Fig. 2. In this model up to three Hund's case (a) states mix to form adiabatic potentials with symmetry $\Omega_\sigma^\pm$ where $\Omega=\Lambda+\Sigma$ is a projection of j ($\vec{j}=\vec{j}_a+\vec{j}_b$) onto the internuclear axis and the $\pm$ describe symmetry with respect to reflection of the electronic coordinates through a plane containing the internuclear axis. The $\Omega_\sigma^\pm$ symmetry follows the Hund's case (c) coupling scheme. For example, within the 0_g^- symmetry the coupling between the $^3\Sigma_g$ and $^3\Pi_g$ ABO's lead to two adiabatic potentials: A purely long-range potential dissociating to the $P_{3/2}+S$ asymptote and a chemically bound potential dissociating to the $P_{1/2}+S$ asymptote. The former potential is extensively studied in the literature [8,13,15] and is a purely long-range potential [31], which possesses inner turning points outside the chemical interaction region and hence only depends on atomic properties such as the fine structure splitting and the atomic ^2S to ^2P transition probability.

The Movre-Pichler model describes the avoided crossings between ABO potentials for internuclear separations where the potential energies are on the order of the ^2P atomic spin-orbit interaction. The Movre-Pichler adiabatic approximation to the electronic Hamiltonians are valid for any of the alkali-metal dimers and could be used to construct a preconditioner for the full eigenvalue problem. However, the model breaks down at small internuclear separations, because at those separations, crossings between the ABO's contributing to a Hund's case (c) symmetry can be diabatic as well. For example, the crossing between the $^3\Pi_u$ and $^1\Sigma_u$ potentials around $7a_0$ changes its character from diabatic for a lithium or sodium dimer to adiabatic for a cesium dimer [23]. Therefore a preconditioner based on the multichannel Hund's case (c) Hamiltonians is preferable. Hence, each block of H_0 is composed of the kinetic-energy operator, the ABO potentials and the ^2P spin-orbit interaction of up to three spin channels depending on the $\Omega_\sigma^\pm$ symmetry. The Green's function $G_0=1/(\mathcal{E}-H_0)$ for each subspace is found by "direct" means

on a single computer, i.e., by inversion or constructed from a direct diagonalization [26]. For example, for the 0_g^- symmetry the interaction between the two ABO's will be included exactly.

The Hamiltonian H_0 for each subspace $\Omega_\sigma^\pm$ of the preconditioner is set up in the Hund's case (a) basis. These subspaces are not uniquely labeled with $\Omega_\sigma^\pm$ but have as additional labels the nuclear spin I and its projection ι. The Hamiltonians of each $\Omega_\sigma^\pm,I,\iota$ subspace differ due to slightly different contributions from the mechanical rotation and hyperfine interactions. This suggests a simpler H_0 and G_0, where all I,ι with $\Omega_\sigma^\pm$ symmetry are replaced by an "average" Hamiltonian. Denoting the Hamiltonian $H_0(\Omega_\sigma^\pm,I,\iota)$ as that part of the total Hamiltonian H that lies within the subspace $\Omega_\sigma^\pm,I,\iota$, the averaged Hamiltonian is

$$H_{\rm ave}(\Omega_\sigma^\pm)=\frac{1}{M}\sum_{I\iota}H_0(\Omega_\sigma^\pm,I,\iota), \qquad (13)$$

where M is the number of allowed I,ι combinations. The corresponding average preconditioner $G_{\rm ave}(\Omega_\sigma^\pm)$ contains identical blocks for different I,ι components. Compared to $H_0(\Omega_\sigma^\pm,I,\iota)$ this approximation breaks down when the total angular momentum F becomes larger and for eigenvalues near the dissociation limits. For large F the molecule starts to spin faster and the nuclear spin loses its locking to the internuclear axis while near the dissociation limits the total nuclear spin I labeling ceases to be a good approximate quantum number. The coupling between the initially weakly coupled $H(\Omega_\sigma^\pm,I,\iota)$ becomes important and the preconditioning, although still converging, is less efficient. In the remainder of the paper we will call G_0 the preconditioner given by $H(\Omega_\sigma^\pm,I,\iota)$ and $G_{\rm ave}$ the preconditioner given by $H_{\rm ave}(\Omega_\sigma^\pm)$.

The two preconditioners are compared in Table I. The energy $\mathcal{E}$ is given in the first column and is with respect to the $P_{3/2}(f_a=3)+S(f_b=2)$ asymptote. At each $\mathcal{E}$ approximately 30 eigenvectors of the Green function $1/(\mathcal{E}-H)$ are evaluated. The density of states for total angular momentum $F=5$ is given in the second column. It increases rapidly with decreasing binding energy and hence indicates the increasing complexity of the problem. All other entries in the table contain the number of vectors n GMRES requires to solve Eq. (10) with residuals smaller than 10^{-12}. Both preconditioners work equally well with the exception of $F=6$ and higher

where G_{ave} does not converge and only G_0 can be used. The number of GMRES vectors increases as the binding energy decreases because hyperfine interactions start to couple the Hund's case (c) symmetries strongly. On the other hand, this table shows that the Hund's case (c) representation of the Na dimer is still sufficient for preconditioning the exact Hamiltonian. The increase of n is not a strictly monotonic function of energy $\mathcal{E}$ but fluctuates on a finer energy scale. This is also due to the approximations made in constructing the preconditioner. The poles of the preconditioner as a function of $\mathcal{E}$ are shifted relative to the exact poles of G and the preconditioner works best if this shift is small. However, choosing $\mathcal{E}$ too close to an eigenvalue of H_0 or H causes large deviations and hence fluctuations in n. Of course near the dissociation limits where the density of states is large this is unavoidable.

The run-time performance of the iterative eigenvalue solver is a complex issue. The G_0 preconditioning is more expensive computationally than the G_{ave} preconditioner. However, the choice of preconditioner does not solely determine the run-time performance. The subspaces are distributed over several computers and with the current generation of computers communication overhead in passing messages quickly dominates. For Na it was found empirically that the best strategy is to use as small a number of computer nodes as possible. This number is mainly determined by the storage of the blocks of the preconditioner G_0. Memory requirements in storing the preconditioner can therefore be important.

The iterative eigenvalue solver returns not only eigenvalues but also eigenfunctions. This allows us to characterize and label the bound states both with exact and approximate quantum numbers. The only exact labels are the total angular momentum F and parity. There are several approximate labels. Each wave function is labeled according to its Hund's case (c) symmetry. In addition, the levels correspond to only one adiabatic Movre-Pichler potential: in essence, a labeling identical to the labeling of the potentials of Fig. 2. This description is approximate and in most cases the dominant symmetry is used to label the state. For states near the atomic hyperfine limits the labeling is somewhat arbitrary. In practice the labeling is not obtained by looking at the wave function directly but by evaluating expectation values of spins and projection operators for a symmetry, i.e., $\Omega_\sigma^\pm$. For example, the expectation value of the electron spin S in the Hund's case (a) representation is

$$\langle S^2 \rangle = \sum_\alpha \int_0^\infty dR \, S_\alpha(S_\alpha+1)|\Psi_\alpha(R)|^2$$

$$= \sum_\alpha \int dy \, S_\alpha(S_\alpha+1)|\phi_\alpha(y)|^2,$$

where α is a sum over all spin degrees of freedom. The vibrational quantum number of a level cannot be easily obtained from a multichannel wave function. The vibrational quantum numbers are instead obtained from eigenvalues of the single-channel adiabatic potentials as defined in Fig. 2. This procedure is valid when the Hund's case (c) coupling scheme is valid.

As an example of our calculations, Fig. 4 shows the multichannel eigenenergies for total angular momentum $F = 5$,
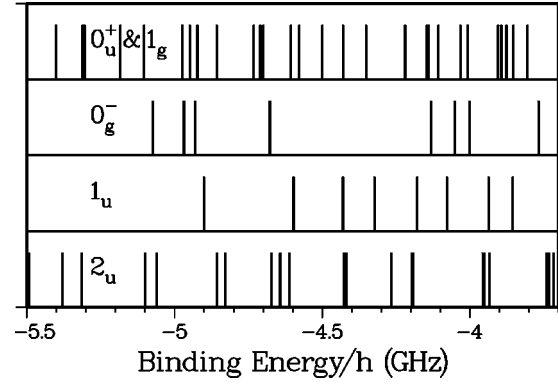
FIG. 4. A stick graph of the Na $P + S$ $F = 5$, $p = 1$ vibrational levels. The binding energies are with respect to the $P_{3/2}(f_a = 3) + S(f_b = 2)$ asymptote. Note that the hyperfine splitting for the ^2S atom is 1.8 GHz. The Hund's case (c) labeling is only approximate where the 0_u^+ and 1_g symmetries are fully broken by the hyperfine mixing.

and parity $p = 1$ about 5 GHz below the $P_{3/2}(f_a = 3) + S(f_b = 2)$ hyperfine asymptote. The ^2S hyperfine splitting is approximately 1.8 GHz and hence strong hyperfine recoupling is expected. The binding energies are converged to a few MHz. The panels of the figure contain levels with the same approximate Hund's case (c) symmetry. The 0_u^+ and 1_g symmetries have merged due to strong hyperfine mixing. An additional example and a more detailed discussion of the mixing is discussed later. The labeling is obtained using the procedure described above. At these binding energies the vibrational spacing that follows from diagonalizing the adiabatic potentials of Fig. 2 is on the order of 1 GHz. For the long-range 0_g^- state the figure shows the four rotational-hyperfine levels of $v = 14$ and 15 and it also shows eight of the ten rotational-hyperfine levels of 1_u $v = 0$. Two vibrational levels of the 2_u symmetry are shown, each having 10 rotational-hyperfine features. For the $0_u^+/1_g$ mixture the situation is more complex. In the absence of coupling between the two Hund's case (c) symmetries there are six and ten rotational-hyperfine levels per vibrational level for the 0_u^+ and 1_g symmetry, respectively. However, these sixteen levels have merged where the figure shows at least two vibrational levels of the two symmetries.

Figure 5(a) shows the radial density of a state with predominantly 1_g symmetry about 10 GHz below the $P_{3/2} + S$ asymptote as a function of the radial coordinate R. The radial density describes the probability of finding the nuclei at internuclear separation R, that is

$$\rho(R) = \sum_\alpha |\Psi_\alpha(R)|^2,$$

where α is a sum over all spin degrees of freedom. This $F = 1, p = -1$ wave function has 53 spin components and is bound by approximately six times the ^2S hyperfine splitting. The outer turning point of the vibrational motion is near $190a_0$ such that the rotational energy $\langle 1_g|\hbar^2 l(l+1)/(2\mu R^2)|1_g\rangle$ is smaller than its hyperfine energy $\langle 1_g|H_{hf}|1_g\rangle$, with H_{hf} the hyperfine contribution to the total Hamiltonian.

The interference pattern of the radial density indicates that this level is a truly multichannel (or nonadiabatic) wave
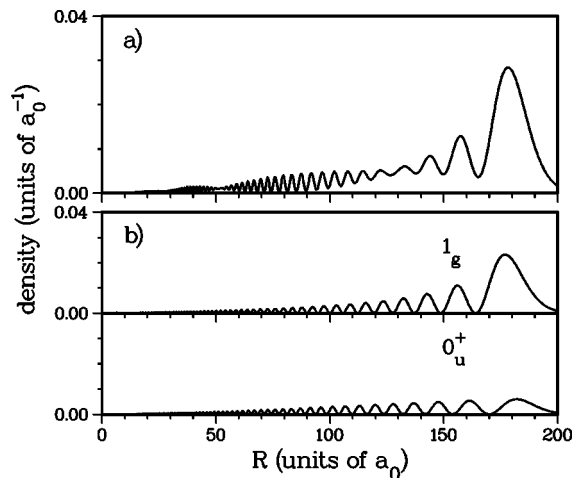
FIG. 5. (a) The radial density of a predominantly 1_g state near the $S + P_{3/2}$ atomic limit as a function of the internuclear separation R. The beating pattern is indicative of nonadiabaticity. (b) The radial density of the same 1_g state separated into the dominant Hund's case (c) symmetries. This 1_g state has 30% 0_u^+ character.

FIG. 6. A $F = 1$, $p = -1$ multichannel wave function in the molecular Hund's case (a) basis. This is a 53 component/channel wave function with a predominantly $J = 2$, 0_g^- character. The top panel shows all components with 0_g^- Hund's case (c) symmetry, the middle panel shows the 2_u components, while the bottom panel shows the remaining components. In addition, the top panel shows components with $^3\Sigma_g$ Hund's case (a) symmetry with full lines and those with $^3\Pi_g$ symmetry with dashed lines. There is about 8% 2_u character.

function. In an adiabatic picture a bound state is described in terms of a single potential and the wave functions have a nodal pattern. The absence of a zero density in Fig. 5(a) therefore implies nonadiabaticity. Figure 5(b) shows the decomposition of this radial density in terms of the relevant Hund's case (c) symmetries. The contributions from the 1_g and 0_u^+ symmetries dominate, with about 30% of the probability distribution in the u state. The strong mixing can be understood from the Movre-Pichler adiabatic potentials of Fig. 2. The attractive 1_g and 0_u^+ potentials run nearly parallel and therefore any nonadiabatic coupling between the two Movre-Pichler potentials is enhanced. In this instance the nonadiabaticity is due to the hyperfine mixing of the 1_g and 0_u^+ symmetries. The vibrational motion on each of the adiabatic Hund's case (c) potentials on the other hand is adiabatic and corresponds to a bound state of the potentials shown in Fig. 2. The hyperfine mixing of 1_g and 0_u^+ symmetries is not accidental and observable for neighboring vibrational levels as well because the vibrational level spacing is comparable to the hyperfine mixing energy.

Figures 6 and 7 show the 53 component wave functions of two nearly degenerate $F = 1$ levels that have predominantly 0_g^- character. The states are again bound by approximately 10 GHz but are separated by only 30 MHz. They belong to the hyperfine structure of the $v = 10, J = 2$ ($\vec{J} = \vec{l} + \vec{S} + \vec{L}$) rovibrational level of the long-range 0_g^- potential dissociating to the $P_{3/2} + S$ limit. The wave functions in Figs. 6 and 7 are nuclear spin $I \approx 1$ and 3 states, respectively. Note that J and I are only approximately good quantum numbers. The wave functions are expressed in the molecular Hund's case (a) representation where the largest components are shown in separate panels. The upper panel shows the Hund's case (a) components with 0_g^- Hund's case (c) symmetry and following the Movre-Pichler model the 0_g^- wave function is an adiabatic mixture of the $^3\Sigma_g$ and $^3\Pi_g$ molecular symmetry. Hence, the radial waves of these components have the same zeros. The middle and bottom panels show that the motions of these levels are not purely adiabatic. A $2_u, I = 2$ level that

lies in between the two levels has a strong influence on the 0_g^- wave functions. However, at a binding energy of -10 GHz strong mixing of the 0_g^- and 2_u symmetries is still accidental. The 0_g^- and 2_u curves have nearly identical long-range behavior, which enhances any nonadiabatic correction, but direct coupling between 0_g^- and 2_u, due to quadrupole hyperfine interactions of the $P_{3/2}$ atom, is too small to explain the observed mixing. The nonadiabatic mixing is due to an indirect process where the 1_g symmetry acts as the intermediate. In fact, coriolis forces mix the 1_g and 0_g^- symmetry and the 1_g and 2_u symmetries are mixed via the hyperfine interactions.

Eigenstates between the $P_{3/2} + S$ and $P_{1/2} + S$ asymptotes are not bound states in the strictest sense of the word. The levels are resonances predissociating into the $P_{1/2} + S$ continuum. In a DVR representation of the dimer these resonances are approximated as bound states by virtue of the zero-boundary condition at R_N. However, as long as a resonance interacts weakly with the continuum the DVR eigenenergies approximate the position of these resonances well. Independent multichannel close-coupling calculations as a function of the collision energy of a S Na atom colliding with a $P_{1/2}$ Na atom show resonance structures in the colli-
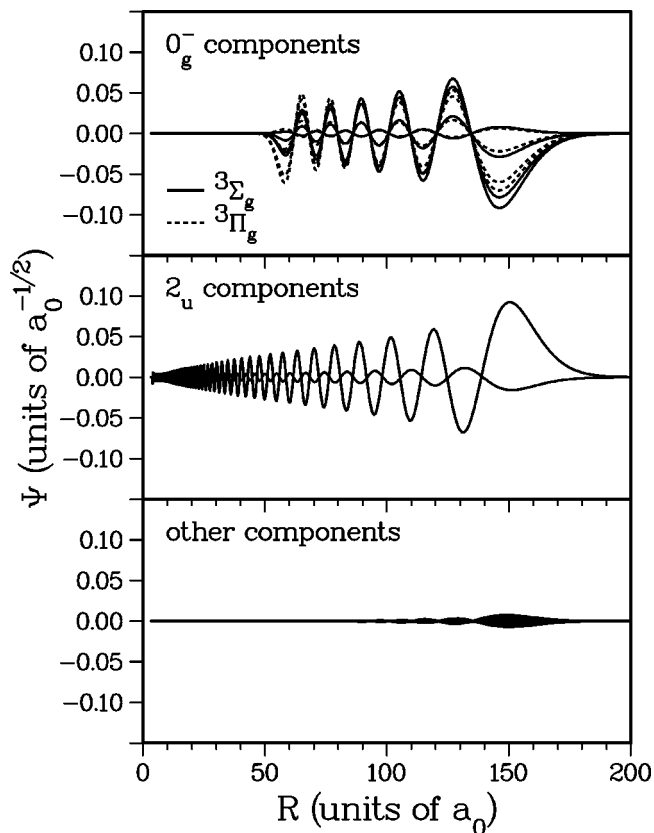
FIG. 7. A second $F=1$, $p=-1$ multichannel wave function in the molecular Hund's case (a) basis. The panels are the same as those described in Fig. 6. This wave function is also a $J=2$, 0_g^- level but has about 25% 2_u character but a slightly different binding energy compared to the wave function in Fig. 6.

sional cross sections near the predicted DVR eigenenergies. For the 1_g and the 0_u^+ symmetry the resonances are a few MHz wide consistent with our inability to converge DVR energies with step and box size to better than a few MHz. The predissociation widths of the purely long-range 0_g^- and 1_u states are negligible.

VI. CONCLUSIONS

We have developed a practical means to evaluate numerically the long-range vibrational wave functions and binding energies of the excited $^2P+^2S$ Na_2 dimer including fine, hyperfine, and rotational structure. The numerical techniques for solving the underlying eigenvalue problem have been described and an impression of the complexity of the eigenvalue spectrum in a region of experimental interest has been given. Near the dissociation limits the bound states form an extremely dense and complex pattern. For those states atomic hyperfine interactions significantly modify the molecular level structure. Moreover, multichannel wave functions with marked nonadiabatic character have been ob-

tained. Deviations from adiabatic behavior prove that the conventional long-range picture of the excited dimer by Movre and Pichler [28] starts to break down near the dissociation limits.

The success of the eigenvalue solver is based on efforts to minimize the size of the discretized Hamiltonian. A nonlinear coordinate transformation of the radial coordinate in combination with a discrete variable representation is implemented to minimize the number of the collocation points. The transformation allows for a smooth transition from small to large step sizes in going from small to large internuclear separations. Since the Na dimer problem involves six coupled spins that generate up to 96 coupled potential surfaces we find that, even with a coordinate transformation, matrix sizes are still too large for using direct diagonalization procedures. An iterative eigenvalue solver with a preconditioner has been implemented. The software is not restricted to the Na dimer but can be used for other alkali-metal dimers as well.

Approximate solutions to the Na_2 bound state problem are essential in constructing a suitable preconditioner for the iterative eigenvalue solver. Good preconditioners can improve the convergence characteristics of the solver dramatically. The effectiveness of two preconditioners has been discussed in detail. The effect of a nonlinear coordinate transformation is investigated in detail using the convergence characteristics of the bound states of a single potential surface.

These computer codes developed for solving the bound state problem have already led to an improved understanding of the Na dimer. The effect of the hyperfine interaction on the rovibrational structure of the purely long-range 0_g^- potential has been quantified [16], enabling the extraction of the most accurate C_3 coefficient and thus the measurement of an accurate ^2P atomic lifetime [13]. Moreover, we were able to prove that retardation has a sizable effect on the level positions. Further analysis of the data will enable us to improve the current value of C_3 in the near future.

Using the codes described in this paper in combination with a close-coupling calculation of the ultracold $^2S+^2S$ collision and a knowledge of the transition dipole moment, a theoretical model of the photoassociation line shape has been constructed for comparing synthetic spectra with experimental photoassociation line shapes. A concise description of this calculation will be given in a future paper. The excellent agreement between theoretical and experimental line shapes made it possible to extract scattering lengths of the $^2S+^2S$ collision [14]. We have also applied the programs towards the understanding of the hyperfine effects on the 1_g potential of ^{87}Rb [32] and the purely long-range 1_u potential of ^{39}K [33].

[1] J. Weiner, Adv. At., Mol., Opt. Phys. **35**, 45 (1995).

[2] P. D. Lett, W. D. Phillips, and P. S. Julienne, Annu. Rev. Phys. Chem. **46**, 423 (1996).

[3] J. Weiner, V. S. Bagnato, S. Zilio, and P. S. Julienne, Rev. Mod. Phys. (to be published).

[4] M. H. Anderson, J. R. Ensher, M. R. Matthews, C. E. Wieman, and E. A. Cornell, Science **269**, 198 (1995).

[5] K. B. Davis, M.-O. Mewes, M. R. Andrews, N. J. Van Druten, D. S. Durfee, D. M. Kurn, and W. Ketterle, Phys. Rev. Lett. **75**, 3969 (1995).

[6] M. Edwards and K. Burnett, Phys. Rev. A **51**, 1382 (1995).

[7] P. D. Lett, K. Helmerson, W. D. Phillips, L. P. Ratliff, S. L. Rolston, and M. E. Wagshul, Phys. Rev. Lett. **71**, 2200 (1993).

[8] R. A. Cline, J. D. Miller, and D. J. Heinzen, Phys. Rev. Lett. **71**, 2204 (1993); **73**, 632 (1994).

[9] L. P. Ratliff, M. E. Wagshul, P. D. Lett, S. L. Rolston, and W. D. Phillips, J. Chem. Phys. **101**, 2638 (1994).

[10] W. I. McAlexander, E. R. I. Abraham, N. W. M. Ritchie, C. J. Williams, H. T. C. Stoof, and R. G. Hulet, Phys. Rev. A **51**, R871 (1995).

[11] D. Leonhardt and J. Weiner, Phys. Rev. A **52**, R4332 (1995).

[12] H. Wang, P. L. Gould, and W. C. Stwalley, Phys. Rev. A **53**, R1216 (1996); H. Wang, X. T. Wang, P. L. Gould, and W. C. Stwalley, Phys. Rev. Lett. **78**, 4173 (1997).

[13] K. M. Jones, P. S. Julienne, P. D. Lett, W. D. Phillips, E. Tiesinga, and C. J. Williams, Europhys. Lett. **35**, 85 (1996).

[14] E. Tiesinga, C. J. Williams, P. S. Julienne, K. M. Jones, P. D. Lett, and W. D. Phillips, J. Res. Natl. Inst. Stand. Technol. **101**, 505 (1996).

[15] H. Wang, J. Li, X. T. Wang, C. J. Williams, P. L. Gould, and W. C. Stwalley, Phys. Rev. A **55**, R1569 (1997).

[16] C. J. Williams, E. Tiesinga, and P. S. Julienne, Phys. Rev. A **53**, R1939 (1996).

[17] S. E. Choi and J. C. Light, J. Chem. Phys. **92**, 2129 (1990).

[18] P. Pendergast, Z. Darakjian, E. F. Hayes, and D. C. Sorenson, J. Comput. Phys. **113**, 201 (1994).

[19] W. Zhu, Y. Huang, D. J. Kouri, C. Chandler, and D. K. Hoffman, Chem. Phys. Lett. **217**, 73 (1994).

[20] R. Wyatt, Phys. Rev. E **51**, 3643 (1995).

[21] J. C. Light, I. P. Hamilton, and J. V. Lill, J. Chem. Phys. **82**, 1400 (1984).

[22] R. Meyer, J. Chem. Phys. **52**, 2053 (1970); D. T. Colbert and W. H. Miller, *ibid.* **96**, 1982 (1992).

[23] O. Dulieu and P. S. Julienne, J. Chem. Phys. **103**, 60 (1995).

[24] D. Sorenson, SIAM J. Matr. Anal. Apps. **13**, 357 (1992); P. Pendergast, Z. Darakjian, E. F. Hayes, and D. C. Sorenson, J. Comput. Phys. **113**, 201 (1994).

[25] R. Barrett, M. Berry, T. Chan, J. Demmel, J. Donato, J. Dongarra, V. Eijkhout, R. Pozo, C. Romine, and H. van der Vorst, *Templates for the Solution of Linear Systems: Building Blocks for Iterative Methods* (SIAM, Philadelphia, 1994). This reference also contains pointers on how to easily use Fortran/C routines to solve for linear systems iteratively.

[26] G. H. Golub, and C. F. van Loan, *Matrix Computations*, 2nd ed. (Johns Hopkins University Press, Baltimore, 1989).

[27] E. Arimondo, M. Inguscio, and P. Violino, Rev. Mod. Phys. **49**, 31 (1977); P. Juncar, J. Pinard, J. Hamon, and A. Chatier, Metrologia **17**, 77 (1981).

[28] M. Movre and G. Pichler, J. Phys. B **10**, 2631 (1977).

[29] S. J. Singer, K. F. Freed, and Y. B. Band, J. Chem. Phys. **79**, 6060 (1983).

[30] B. Gao, Phys. Rev. A **54**, 2022 (1996).

[31] W. C. Stwalley, Y-H. Uang, and G. Pichler, Phys. Rev. Lett. **41**, 1164 (1978).

[32] C.-C. Tsai, D. Heinzen, E. Tiesinga, P. S. Julienne, Y. Huang, and D. Hoffman (unpublished).

[33] X. T. Wang, H. Wang, P. L. Gould, W. C. Stwalley, E. Tiesinga, and P. S. Julienne Phys. Rev. A **57**, 4600 (1998).